Transformerless Split-Inductor Neutral Point Clamped Three-Level PV Grid-Connected Inverter

Huafeng Xiao, *Student Member, IEEE*, and Shaojun Xie, *Member, IEEE*

Abstract—Characterized by low leakage current and low voltage stress of the power device, a neutral point clamped three-level inverter (NPCTLI) is suitable for a transformerless photovoltaic (PV) grid-connected system. Unfortunately, the shoot-through problem of bridge legs still exists in an NPCTLI, so its operation reliability is degraded. An improved three-level grid-connected inverter is proposed based on the NPCTLI and the dual-buck half-bridge inverter (DBHBI), and which avoids the shoot-through problem. The proposed topology guarantees no switching-frequency common-mode voltage and no shoot-through risk. Furthermore, the freewheeling diode of bridge legs of the DBHBI can be removed taking into consideration the unity power factor of grid current, and a straightforward topology is thus derived. The new topology is referred to as split-inductor NPCTLI (SI-NPCTLI). The operation mode, common-mode characteristic, and control strategy are analyzed. Finally, both the simulation and the experimental results of a 1-kW SI-NPCTLI prototype verify the analysis.

Index Terms—Dual-buck half-bridge inverter (DBHBI), neutral point clamped three-level inverter (NPCTLI), photovoltaic (PV) grid-connected inverter, transformerless.

I. INTRODUCTION

THE PHOTOVOLTAIC (PV) power generation system is playing an important role in the development of distributed electric power systems [1]. In order to achieve low cost and compactness, as well as increased reliability and efficiency, the concept of the transformerless PV grid-connected inverter was proposed [2]. In recent years, the transformerless PV grid-connected inverters (TLI), already well-accepted in European markets, have draw more and more attention in other parts of the world [3]–[5], [7]–[10]. Key issues related to TLI are leakage-current suppression and reliability improvement [1]. Depending on the inverter topology, there exist potential fluctuations between the solar cell array and the ground, and the fluctuations are square-wave voltages at the switching frequency. Due to the galvanic connection between power grid and solar cell array, the stray capacitors to ground formed by the surface of the PV array form a path for the leakage current. Energized by a fluctuating potential, the stray capacitors lead to leakage currents. A person,

connected to the ground and touching the PV array, may conduct the capacitive current to the ground, causing an electrical hazard. At the same time, the conducted interference and radiated interference are brought in by the leakage current; furthermore, the in-grid current harmonics and losses are increased.

Neutral point clamped three-level inverter (NPCTLI) [6] is widely adopted in a transformerless PV system [4], [5], [8], [10]. The NPCTLI's topology can overcome the problems of leakage current and restrict the dc component injected to the grid [8]. In [7] and [9], an analysis model for the leakage current of a transformerless PV grid-connected inverter was presented in detail, which can provide the theoretical support for the leakage-current-suppression technique. With this model, the application of a single-phase NPCTLI in PV grid-connected system was thoroughly studied in [8], and an analysis of the principles and characteristics of leakage current elimination in an NPCTLI were provided. Worth noting, NPCTLI also suffer from shoot-through risk as do other bridge-type inverters, which is a major obstacle to the reliability for power-conversion system. So, it is worth considering reliability enhancements to NPCTLIs.

A dual-buck half-bridge inverter (DBHBI) was proposed in [11], which received considerable attention in recent years [12]–[17]. The DBHBI can avoid the shoot-through problem, the freewheeling current flows through the independent freewheeling diodes instead of the external well-matched freewheeling diodes of the switches, and all the switches and diodes are operated at half of the line cycle; so, the efficiency can be improved due to no biased current. But the DBHBI can only work with the bipolar modulation strategy, and there is large voltage stress on the power devices. In order to solve the aforementioned problems, the multilevel leg structure was introduced [18]–[20], which can work with the unipolar modulation strategy and reduce the voltage stress effectively [16].

Based on the half-bridge-type transformerless PV grid-connected inverter, a novel split-inductor NPCTLI (SI-NPCTLI) with variable hysteresis band fixed-frequency control is proposed in this paper. There are no leakage current and shoot-through problems in the proposed inverter. The voltage stress of power devices in an SI-NPCTLI is the same as in an NPCTLI, and an SI-NPCTLI can be also operated with unipolar modulation. The variable hysteresis band fixed-frequency control offers an excellent current reference tracking performance and fast transient response ability in comparison with other current controllers. Furthermore, the independent freewheeling diode of the DBHBI can be removed considering the unity power factor of the grid current, and the operation safety is ensured by shut down of the high-frequency switching drive signal ahead of the current drops to zero. Based on single-phase structure, the

H. Xiao is with the College of Electrical Engineering, Southeast University, Nanjing 210096, China (e-mail: saloulin@ynet.com).
S. Xie is with the College of Automation Engineering, Nanjing University of Aeronautics and Astronautics, Nanjing 210016, China (e-mail: eeac@nuaa.edu.cn).

SI-NPCTLI can be easily extended to a three-phase four-line transformerless grid-connected inverter with high reliability and low leakage current characteristics as well.

The circuit topology, operation principle, and common-mode characteristic of the SI-NPCTLI, and the comparison among several inverters are presented in Section II. The control strategy of the proposed inverter is analyzed in Section III. Simulation results including steady, dynamic, maximum power point tracking (MPPT), and shoot-through fault are presented in Section IV. In Section V, the experimental results of a 1-kW SI-NPCTLI single-phase grid-connected inverter prototype verify the theoretical analysis of Section II. Finally, concluding remarks are given in Section VI.

II. CONSTRUCTION AND FEATURE ANALYSIS OF AN SI-NPCTLI

A. Construction of an SI-NPCTLI

As shown in Fig. 1(a), the power switches in the DBHBI with a diode-clamped three-level switch cell being substituted, and the independent freewheeling diodes of the DBHBI being omitted, a novel topology that is compact and similar to NPCTLI is derived. The earth connection point is the important detail in this topology, while the midpoint of PV cluster does not earth, the output end of the SI-NPCTLI can be connected to the grid freely; otherwise, once the midpoint of PV cluster earths, both the midpoint of capacitor's bridge leg and the midpoint of PV cluster must be connected to the neutral line of the grid. In Fig. 1(a), the instantaneous voltage across points 1 and 3 is defined as u_{13} and the instantaneous voltage across points 2 and 3 is defined as u_{23}. In Fig. 1(b), waveforms of the switch driving signals and the output current of the SI-NPCTLI are illustrated.

B. Operation Principle

The switches of the DBHBI are modulated at half of the line cycle, so the switching and conduction losses are reduced and the efficiency can be improved [17]. The proposed SI-NPCTLI is modulated at half of the line cycle current as well. Before analysis, the following assumptions are given: 1) all power switches and diodes are the ideal devices with ignored switching time and conduction voltage drop; 2) all inductors and capacitors are ideal, and $C_{dc1} = C_{dc2}$, $L_1 = L_2 = L$; and 3) the inverter operates at the unity power factor, i.e., the inductor current i_{L12} is in phase with the grid voltage u_g. Taking the operation during the half-cycle of the positive grid voltage, e.g., the detailed analysis of the inverter operation modes is described. The operation during the negative half-cycle is similar to the positive one.

1) Mode 1: With switches S_1 and S_2 ON, and S_3 and S_4 OFF, the output voltage of the bridge leg is the voltage of capacitor C_{dc1}, i.e., $u_{13} = (1/2)U_{pv}$. At this duration, i_{L1} indicating the current of inductor L_1 increases

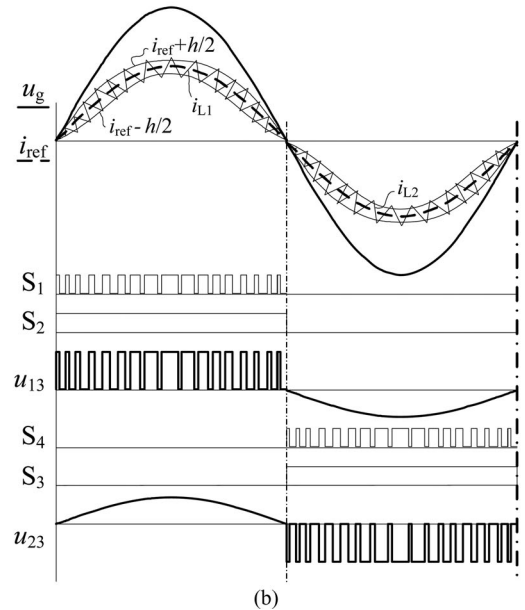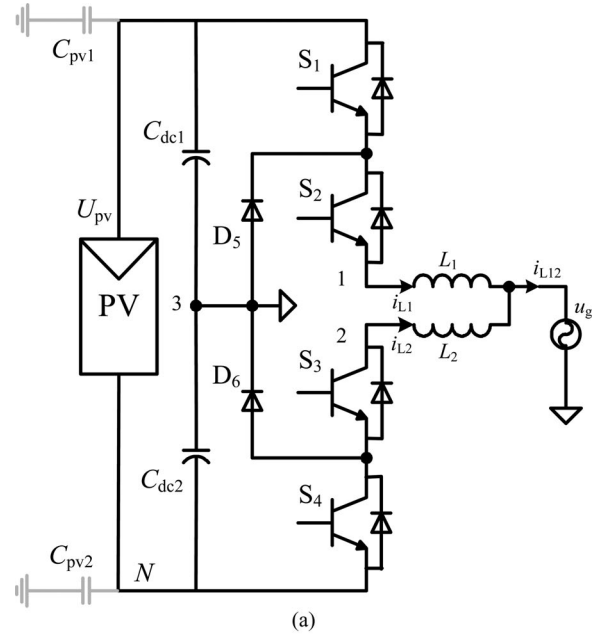$$L\frac{di_{L1}}{dt} = \frac{1}{2}U_{pv} - u_g. \qquad (1)$$

Fig. 1. Split-inductor neutral point clamped three-level PV grid-connected inverter. (a) Power stage. (b) Key waveforms and driving signals.

2) Mode 2: With S_1 OFF, S_2 ON, and S_3, S_4 still OFF, the voltage on S_1 is clamped to the half of the input voltage by the diode D_5, and the output voltage of the bridge leg is zero, i.e., $u_{13} = 0$. At this duration, the current of inductor L_1 states in the freewheeling stage and i_{L1} decrease

$$L\frac{di_{L1}}{dt} = 0 - u_g. \qquad (2)$$

So, during the positive half-cycle of the grid voltage, the output-voltage levels of the bridge leg include zero and $(1/2)U_{pv}$. Similarly, during the negative half-cycle, the output voltage gets the two levels of zero and $-(1/2)U_{pv}$. As compared with the DBHBI, which only has the two levels, $(1/2)U_{pv}$ and

TABLE I
OPERATION LEVELS OF THE SI-NPCTLI

		v_{1N}	v_{2N}	v_{3N}	v_{DM}	v_{CM}	$v_{CM\text{-}DM}$	$v_{CM}+v_{CM\text{-}DM}$
Positive	Mode 1	U_{pv}	$u_g+U_{pv}/2$	$U_{pv}/2$	$U_{pv}/2$	$3U_{pv}/4$	$-U_{pv}/4$	$U_{pv}/2$
$i_{L12}>0$	Mode 2	$U_{pv}/2$	$u_g+U_{pv}/2$	$U_{pv}/2$	0	$U_{pv}/2$	0	$U_{pv}/2$
Negative	Mode 3	$u_g+U_{pv}/2$	0	$U_{pv}/2$	$-U_{pv}/2$	$U_{pv}/4$	$U_{pv}/4$	$U_{pv}/2$
$i_{L12}<0$	Mode 4	$u_g+U_{pv}/2$	$U_{pv}/2$	$U_{pv}/2$	0	$U_{pv}/2$	0	$U_{pv}/2$

Note: In the negative half-cycle, S_1, S_2 is off, and S_3, S_4 is on with operation mode 3. S_1, S_2 is off, S_3 is on, and S_4 is off with operation mode 4.
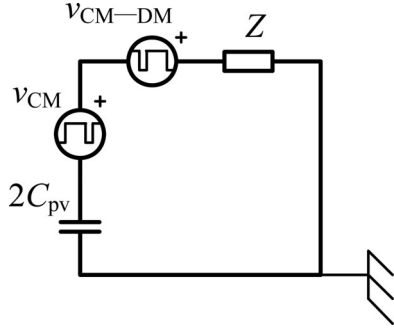

Fig. 2.   Simplest common-mode model for a single-phase grid-connected inverter at the medium-frequency range [7], [9].

TABLE II
COMPARISON AMONG THE SI-NPCTLI AND OTHER INVERTERS

		NPCTLI	DBHBI	SI–NPCTLI
Switches	Number	4	2	4
	$U_{DS}(p)$ /V	400	800	400
	I_D(rms) /A	2.16/2.95	2.54	2.16/2.95
	SDP /kVA	4.088	4.064	4.088
Diodes	Number	2	2	2
	$U_{KA}(p)$ /V	400	800	400
	I_A(rms) /A	0.93	0.47	0.93
	SDP /kVA	0.744	0.752	0.744
Total SDP /kVA		4.832	4.816	4.832
Inductor	Number	1	2	2
	I_L(rms) /A	4.17	2.95	2.95
	L /mH	4	16	4
Shoot-through problem?		Yes	No	No
Leakage current?		No	No	No

Note：U_{pv}=800V, u_g=339sin(314×t), P=1000W, the maximum band width of current hysteresis H(max)=1.25A.

$-(1/2)U_{pv}$, the SI-NPCTLI can reduce the current ripple of the inductor dramatically, and it is benefit to reduce the inductance.

C. Analysis of Common Mode Characteristic

The switching frequency common-mode voltage of a transformerless PV grid-connected inverter is the source of the leakage current coming forth [7]–[9]. Therefore, whether the switching frequency common-mode voltage appears or not is the evaluation criterion for the topology used in a transformerless PV grid-connected system. Fig. 2 shows the simplest common-mode model for the SI-NPCTLI; for its deductive process refer to [7] and [9]. Because the inductor current has different paths in the positive and negative half-cycles, there are also differences in calculating the differential-mode and common-mode voltages in the SI-NPCTLI. In the positive half-cycle

$$v_{CM} = \frac{v_{1N}+v_{3N}}{2} \tag{3}$$

$$v_{DM} = v_{1N}-v_{3N} \tag{4}$$

In the negative half-cycle

$$v_{CM} = \frac{v_{2N}+v_{3N}}{2} \tag{5}$$

$$v_{DM} = v_{2N}-v_{3N} \tag{6}$$

The term v_{CM-DM} represents the influence of the differential-mode voltage to the common-mode voltage [7], [9]

$$v_{CM-DM} = -\frac{v_{DM}}{2}. \tag{7}$$

Table I shows the operating levels of the SI-NPCTLI. It is found in the last column of Table I (with the shadow) that the total common voltage produced by the SI-NPCTLI is a constant

TABLE III
PARAMETERS OF THE SIMULATION MODEL AND THE PROTOTYPE

Parameter	Value
Input voltage/V	800
Grid voltage/V, Frequency/Hz	240/50
Rating Power /W	1000
DC Capacitor C_{dc1}, C_{dc2}/μF	470μF/450V
Power Device S1~S6 (MOSFETs)	IXFN36N100
Filter Inductance L_1、L_2/ mH	4
Common-mode Inductance L_{CM}	Core：2×2W-43615-TC Wire：2mm Turns：10+10
Common-mode Capacitance C_{Y1}, C_{Y2}/nF	2.2
Parasitic Capacitance C_{pv1}, C_{pv2}/μF	0.1

value and it will not introduce leakage current in transformerless PV grid-connected applications [7]–[9]. Compared with the common-mode character of the NPCTLI presented in [7], it can be found that the SI-NPCTLI and NPCTLI have the same common-mode performance.

D. Comparison With Several Topologies

In this section, the quantitative comparison among the SI-NPCTLI, NPCTLI, and DBHBI from several aspects are discussed. As shown in Table II, including the number of power devices, voltage and current stress, and switching device power (SDP) factor, which is presented to scale the power level of switching devices [21], as well as the performance included the shoot-through and leakage-current problems. The comparison of passive components mainly focuses the amount and the value of the filter inductor. The electrical parameters are shown in Table III.
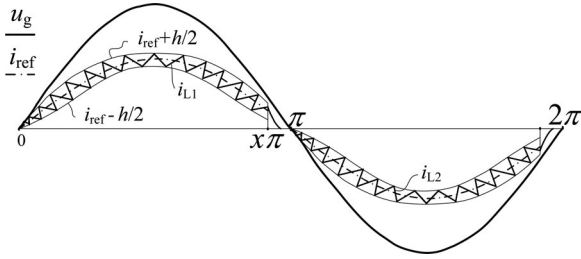
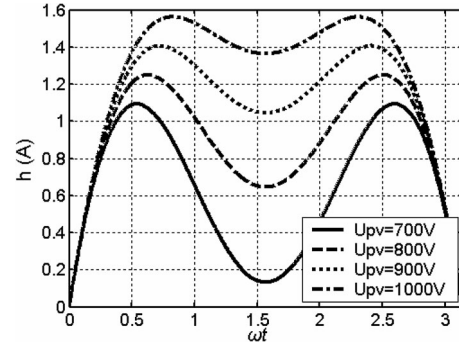Fig. 3.   Phase control of inductor current i_{L12}.

Fig. 4.   Curves of the hysteresis band with constant switching frequency under different PV voltage ($u_g = 339\sin(314 \times t)$; $L = 4$ mH; $f_s = 20$ kHz).

It can be seen from Table II that the DBHBI is in a weak position at devices stress and the value of inductance, while the NPCTLI is in a well position at the quantity of the filter inductor, and with the largest inductor current stress. However, the shoot-through problem makes the NPCTLI in a weak position. The proposed SI-NPCTLI is completely dominant over the DBHBI. Compared with the NPCTLI, the SI-NPCTLI has the advantages of reduced inductor current stress and, most importantly, no shoot-through problem except the duple filter inductors. The three circuit topologies are comparable with regard to total SDP. As they all do not generate high-frequency time-varying common-mode voltage when applied to a transformerless PV grid-connected inverter, the leakage current is restrained.

III. Control Strategy of an SI-NPCTLI

A. Analysis of the Hysteresis Band

The analysis in Section II-B assumes that the inverter works with the unity power factor, i.e., the inductor current i_{L12} is in phase with the grid voltage u_g. This assumption is reasonable under the requirement of the unity power factor between the in-grid current and the grid voltage, when applied to a PV grid-connected inverter. However, as the freewheeling diodes of bridge leg in the DBHBI are omitted, in order to ensure safe operation, the inductor current needs to be reliably dropped to zero before the zero crossing of the grid voltage.

The hysteresis current control can achieve accurate tracking to the inductor current [22]. In order to ensure the zero inductor current before the zero crossing of the grid voltage, the high-frequency switching signals must be stopped at the time $x\pi$, and the inductor current may be forced to zero by the grid voltage, as shown in Fig. 3.

The time $x\pi$ to turn OFF the high-frequency switching signals is expressed as

$$\frac{\int_{x\pi}^{\pi} [U_g \cdot \sin(\omega t) + U_D(\text{ON}) + U_S(\text{ON})]}{L} \geq I_{\text{ref}} \cdot \sin(x\pi) + \frac{h}{2}. \tag{8}$$

Here, $U_D(\text{ON})$ and $U_S(\text{ON})$ are the ON-state voltages of the clamping diodes and the power switches, respectively, h is the bandwidth of current hysteresis, i.e., the ripple of inductor current, and x is the percent of high-frequency driving signal continuance.

Hysteresis current control, which is a nonlinear control method, possesses high performance, simple realization circuit,

high stability, inherent current-limiting capability, and fast dynamic response. However, due to the unfixed switching frequency, the energy of spread-spectrum of output current is widely distributed. As a result, it is difficult to design the filter. Numerous studies have focused on this problem [23]–[28], and hysteresis band real-time regulation is one of the most effective ways to follow.

For the proposed SI-NPCTLI, from (1) and (2), one can get

$$h = \frac{u_g(U_{\text{pv}} - 2 \cdot u_g)}{U_{\text{pv}} \cdot L \cdot f_s}. \tag{9}$$

Here, f_s is the expected switching frequency. Fig. 4 shows the curves of hysteresis band under different PV voltage according to (9) in the half-cycle of grid. So, when the inverter is operating, the fixed frequency hysteresis control can be fulfilled by calculating the hysteresis band h using the transient value of the grid voltage and output voltage of PV array.

Furthermore, the time $x\pi$ to turn OFF the high-frequency switching signals can be redesigned considering the antislanding requirements. At the islanding mode, when the detected voltage frequency is increasing, reduce the time of $x\pi$ (namely increasing the gap of current reference) in a positive-feedback manner, to trip the over-frequency limitation. Detailed designing and experimental verification will be demonstrated in another paper.

With the aforementioned control method, the single-phase SI-NPCTLI can be extended to three-phase four-line grid-connected inverter structure, as shown in Fig. 5. It can be decomposed into three independent single-phase inverters completely and possesses the same operation safety performance and low leakage current characteristics. In the three-phase topology, the midpoint of PV cluster can earth, or not. In addition, while in the absence of accessible star center, such as Δ-way grid, the proposed three-phase topology is not employed.

B. Control Strategy of an SI-NPCTLI

Considering the proposed SI-NPCTLI for PV grid-connected applications, the schematic control block is shown in Fig. 6.

In Fig. 6, the phase and the amplitude of grid voltage and the PV array voltage are sampled by the digital signal processing (DSP) chip. The reference current $i_{L12}(\text{ref})$ of the inductor
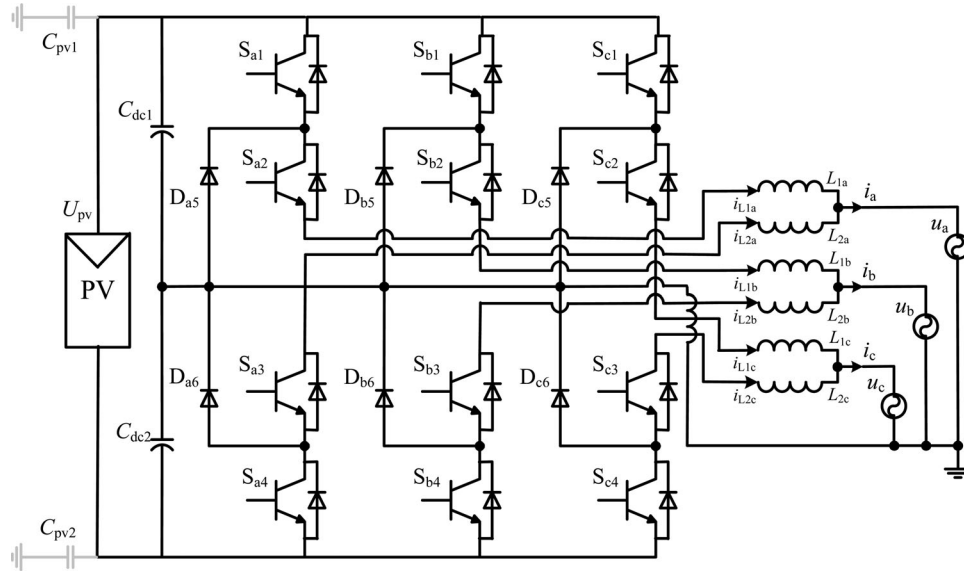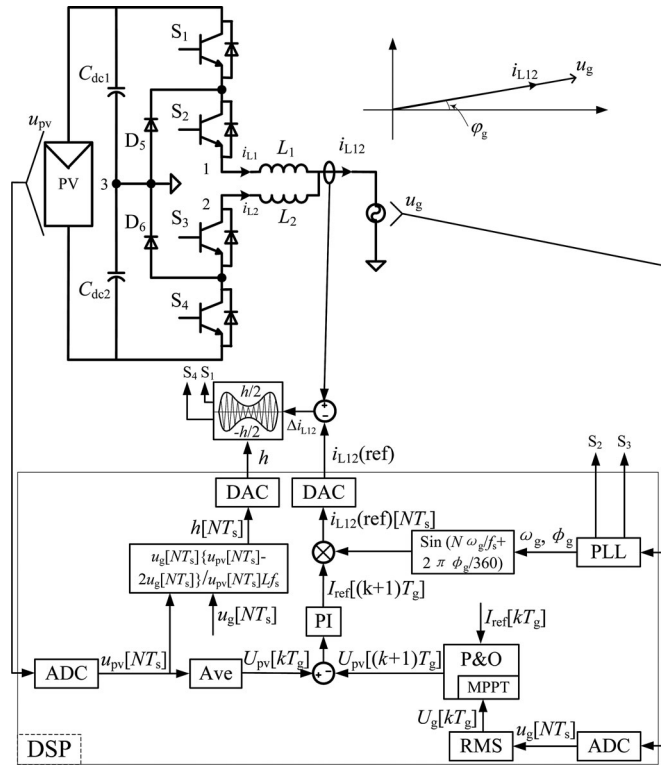
Fig. 5. SI-NPCTLI three-phase inverter with neutral.

Fig. 6. Control block of SI-NPCTLI PV grid-connected inverter (T_s is the switching period; T_g is the grid period; ω_g is the angular frequency of grid voltage; and ϕ_g is the initial phase angle of grid voltage)..

current i_{L12} can be obtained by calculating the product of the reference amplitude I_{ref} and the phase of the grid voltage. As the result of hysteresis current control, the inductor current i_{L12} can achieve the error-free tracking to the reference current. Then, the MPPT algorithm can be fulfilled by calculating U_g and reading I_{ref}. Lastly, the driving signals of the inverter can be generated by comparing the real-time hysteresis band h with the error of

inductor current i_{L12} and reference current $i_{L12}(\text{ref})$ provided by DSP.

IV. SIMULATION ANALYSIS

A simulation model of the single-phase grid-connected SI-NPCTLI has been established with MATLAB/Simulink. Table III shows the simulation parameters.

A. Validation of Steady-State Characteristics

When the single-phase grid-connected SI-NPCTLI operates under the hysteresis current control with a fixed band, the waveforms of the grid current and voltage and the energy spectrum of the grid current are shown in Fig. 7. Fig. 8 shows the same terms of the condition under the variable band hysteresis current control. From the energy spectrums of the inductor current i_{L12} in Figs. 7(b) and 8(b), it can be seen that the current harmonic concentrates to the desired frequency band by calculating the hysteresis band h real time, and it will be easier to be further filtered.

Refer to the curves of the inductor current i_{L12} and grid voltage u_g in Fig. 9, hysteresis control and stopping the high frequency switching signals ahead make the current i_{L12} zero before the zero crossing of u_g, which ensures the current path-shifting safety.

From Fig. 9, it can be also found that the inductor current i_{L12} achieves the capability of high-precision tracking to the given reference. For the grid-connected applications, the performance of current tracking under different grid-current reference, especially light-load and zero-grid-current reference tracking performance (such as the max utility backfeed current, which is must be limited in many international standards, such as UL1741 and NEC690), is the key index to evaluate the inverter control and safety features. Fig. 10(a)–(c) shows the operation waveforms under different grid-current reference of the single-phase grid-connected SI-NPCTLI, respectively. It can be seen, when
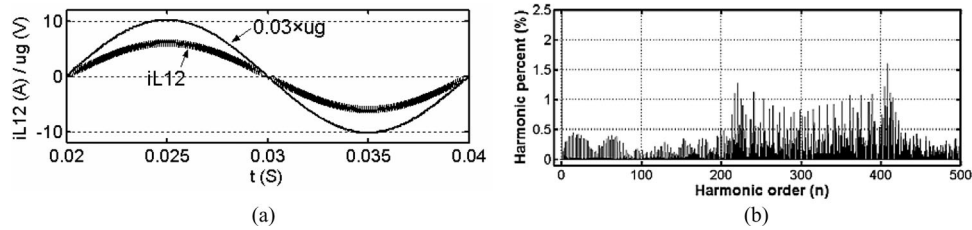
Fig. 7. Fixed-band hysteresis current control for the SI-NPCTLI. (a) Grid current and grid voltage. (b) Energy spectrum of the grid current.
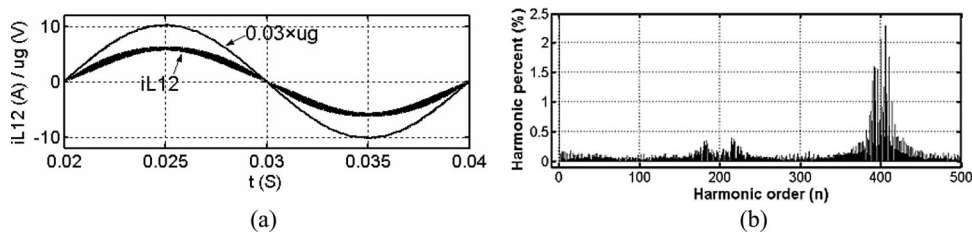

Fig. 8. Variable hysteresis band constant-frequency control for the SI-NPCTLI. (a) Grid current and grid voltage. (b) Energy spectrum of the grid current.
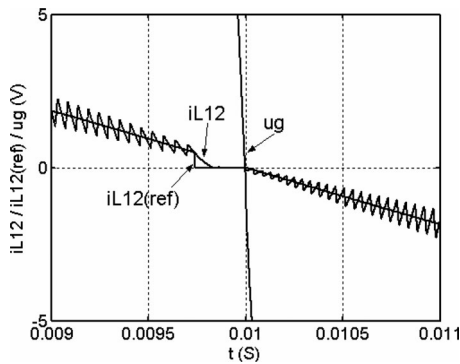

Fig. 9. Current path change at the grid-voltage crossover.

the grid-current reference is reduced and less than the hysteresis band ($h/2$), the high-frequency switching signals turn OFF, as shown in Fig. 10(b). As a result, the quality of the grid current worsens. However, the decreased switching times improves the converter efficiency at light load. Fig. 10(c) shows the waveforms of the inverter working under the zero-grid-current reference. As a result of this, the grid-current reference is always less than the hysteresis band and the converter acts no high-frequency switch actions, which ensures high precision tracking to the grid-current reference and, furthermore, realizes the zero max utility backfeed current.

B. Verification of the Dynamic Performance

Fig. 11 shows the dynamic response waveforms of the single-phase grid-connected SI-NPCTLI under the variable bandwidth hysteresis current control, when the grid-current reference i_{L12}(ref) rises and drops suddenly. It can be seen that the SI-NPCTLI represents a very good dynamic response performance. When the grid voltage and PV input voltage change suddenly, variable-band hysteresis current control arithmetic can realize constant-frequency control by changing the hysteresis band h rapidly, as shown in Fig. 12(a) and (b), respectively.

C. Verification of MPPT

The model of the PV array with the MPPT algorithm was implemented in Simulink, operated at various irradiations and constant cell temperature. The PV array was modeled by a constant voltage source in series with resistor for simplicity and speediness in our simulation model. Fig. 13 shows the simulation results of increasing and decreasing irradiation; the oscillation of MPP voltage is brought due to power ripple of single-phase grid-connected inverter. It can be seen that the MPPT algorithm can track the MPP of PV array within 1.5 times grid period, so the adopted MPPT algorithm is valid.

D. Verification of the Shoot-Through Fault

The proposed SI-NPCTLI has no shoot-through risk as analyzed in Section II. In order to support this point, the comparative simulation results of the SI-NPCTLI and NPCTLI are presented in Fig. 14. When the shoot-through durations (about 10 μs) appear at the zero crossing and peak of the grid voltage, respectively, the current through power devices is limited by the SI in the SI-NPCTLI. However, the current through power devices rapidly increases as shoot-through appearance in the NPCTLI; its amplitude can be seen from Fig. 14(b), which would destroy the devices.

V. EXPERIMENTAL ANALYSIS

In order to verify the validity of the proposed SI-NPCTLI and to evaluate the performance of the leakage-current suppression, a universal prototype inverter has been fabricated in our laboratory, as shown in Fig. 15. Main electrical parameters and component parameters are shown in Table III. In Fig. 15, the module labeled "universal three-level inverter" represents the NPCTLI or SI-NPCTLI structure. C_X denotes differential-mode capacitors in the electromagnetic interference (EMI) filter; L_{DM} and L_{CM} are the differential-mode and common-mode inductors, respectively; and C_{Y1} and C_{Y2} are the common-mode capacitors.
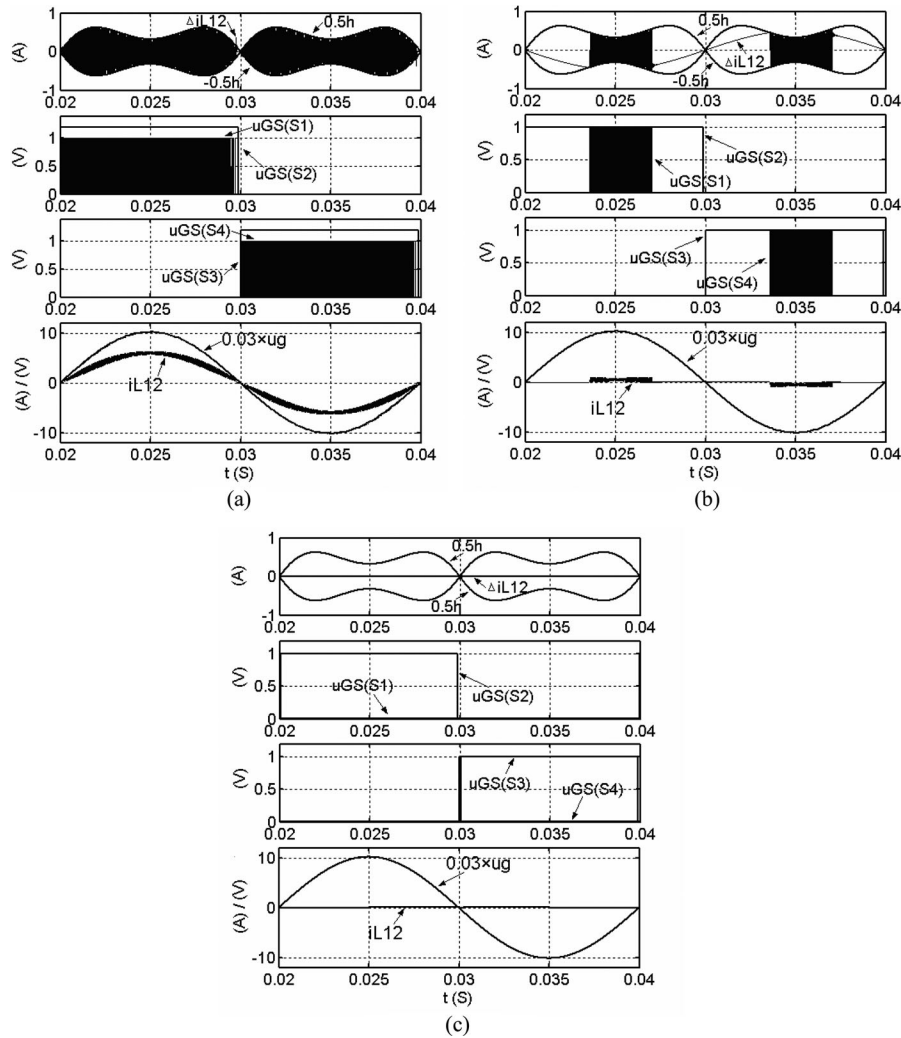
Fig. 10. Steady operation waveform with different grid-current command under variable-band constant-frequency hysteresis current control. (a) Rated current. (b) 5% of the rated grid current. (c) zero-grid-current reference.
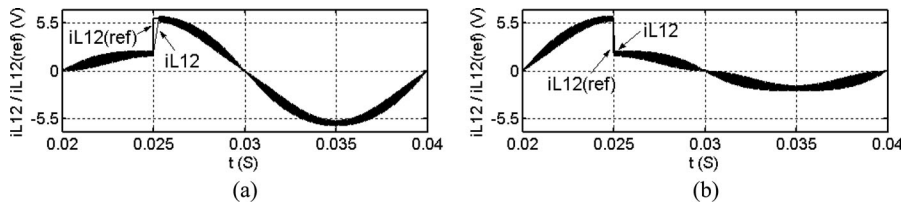

Fig. 11. Dynamic response of the grid current under variable-band constant-frequency hysteresis current control. (a) Grid current rises from 2 to 6 A. (b) Grid current drops from 6 to 2 A.
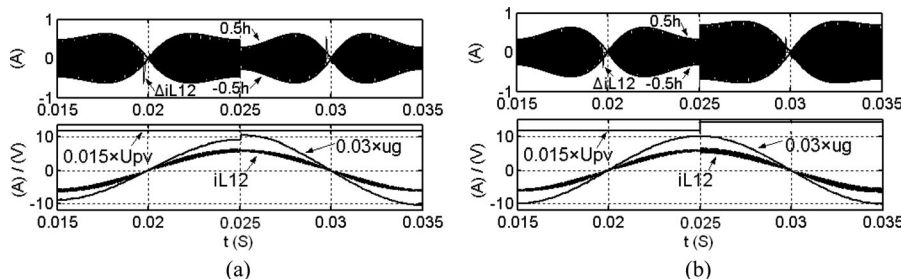

Fig. 12. Dynamic response of the grid voltage and PV input voltage under the variable-band constant-frequency control algorithm. (a) Grid voltage rises from 300 to 350 V. (b) PV input voltage rises from 800 to 1000 V.
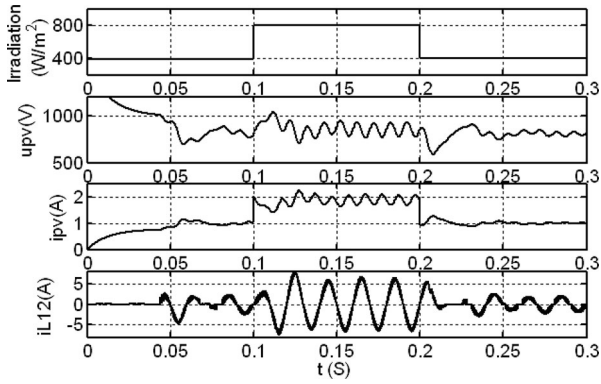
Fig. 13. Simulated results for the MPPT algorithm. From top to down: sun irradiation, voltage of the PV module, output current of the PV module, and in-grid current.
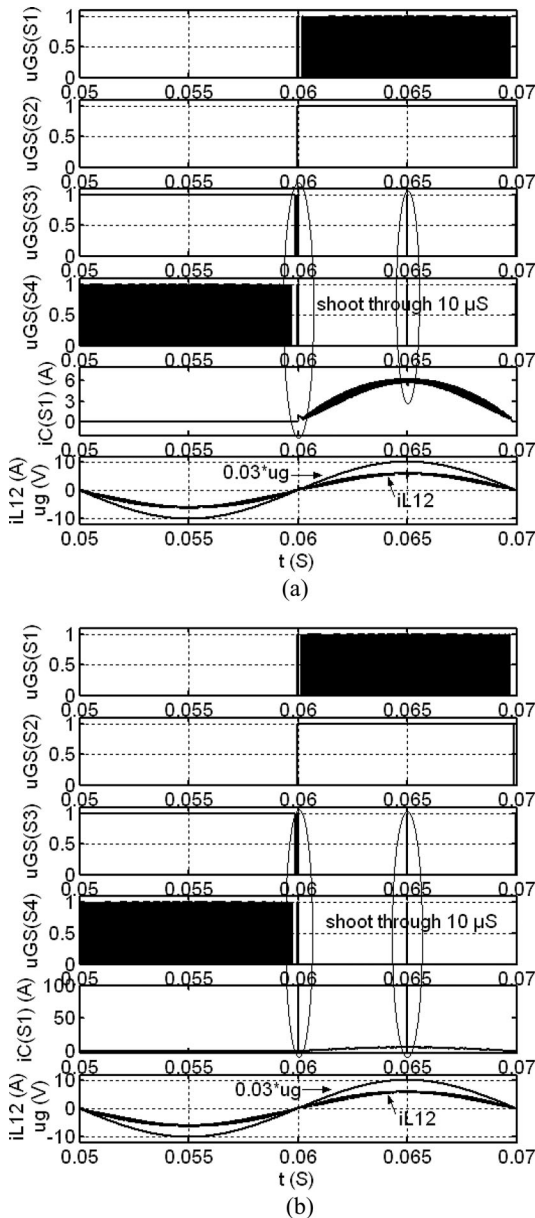

Fig. 15. Test layout.

Fig. 14. Simulation results of the shoot-through fault by EMI noise's misgating-on in the SI-NPCTLI and NPCTLI. (a) SI-NPCTLI. (b) NPCTLI.
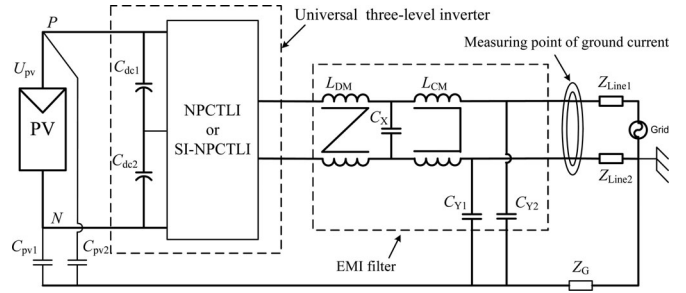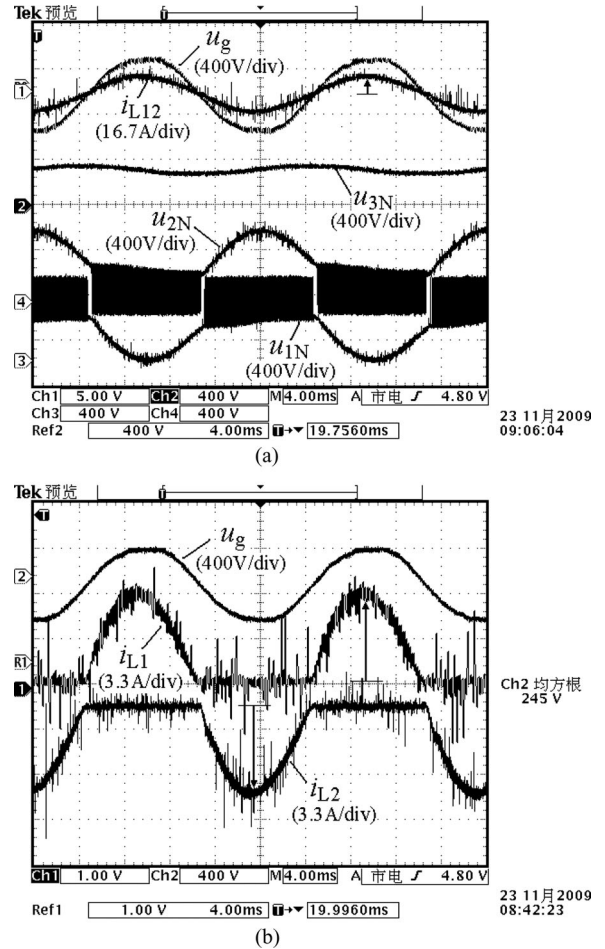

Fig. 16. Experimental waveforms of the bridge-leg voltage, grid voltage, and inductor current in the SI-NPCTLI. (a) Grid voltage u_g, in-grid current i_{L12}, and voltage u_{1N}, u_{2N}, and u_{3N} between bridge-legs and point N. (b) Filter inductor current i_{L1} and i_{L2} and the grid voltage u_g.

The stray capacitances C_{pv1} and C_{pv2} between solar panels and the earth depend on the material and size of the solar panels, soil properties, air humidity, installation, etc. Z_{Line1} and Z_{Line2} are line impedances (mainly inductive). Z_G is the impedance between grid ground and chassis ground of the inverter.

Experimental studies focused on the operation principle verification of the proposed topology and the leakage-current performance testing and comparison. For the convenience of experimental testing, the solar array is simulated by an adjustable dc source and the additional high-voltage ceramic capacitors
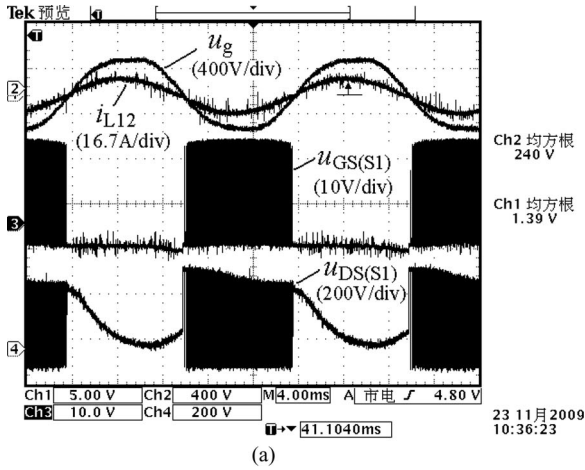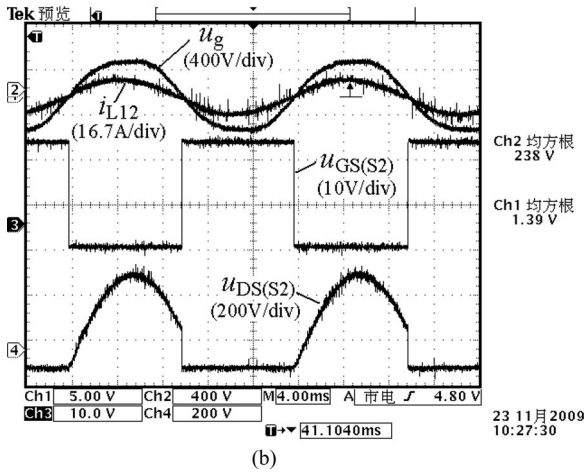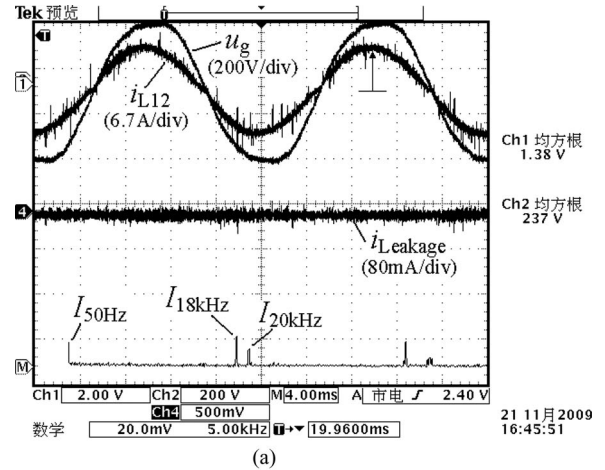
Fig. 17. Experimental waveforms of driving, voltage across the drain and source of switch, grid voltage, and in-grid current in the SI-NPCTLI. (a) Driving $u_{GS(S1)}$ and drain–source voltage $u_{DS(S1)}$ for the switch S_1, grid voltage u_g, and in-grid current i_{L12}. (b) Driving $u_{GS(S2)}$ and drain–source voltage $u_{DS(S2)}$ for the switch S_2, grid voltage u_g, and in-grid current i_{L12}.

Fig. 18. Experimental waveforms of the grid voltage u_g, in-grid current i_{L12}, leakage current $i_{Leakage}$, and energy spectrum of leakage current in the SI-NPCTLI and NPCTLI ($I_{50\,Hz}$ represents the common-mode current produced by the grid voltage; $I_{18\,KHz}$ represents the common-mode current produced by the PV cells simulator; $I_{20\,KHz}$ represents the common-mode current produced by the grid-connected inverter). (a) SI-NPCTLI. (b) NPCTLI.
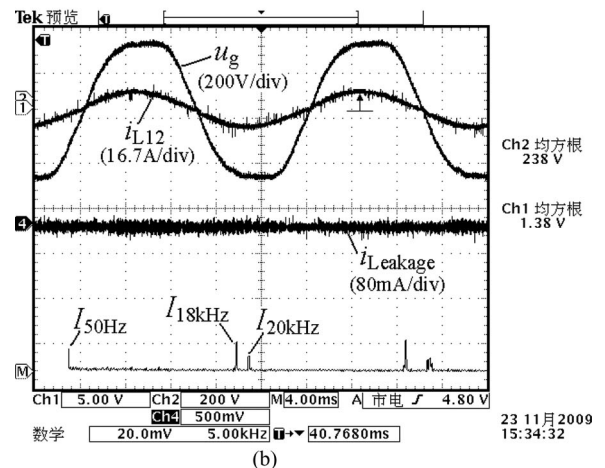
C_{pv1} and C_{pv2} (100 nF, for the 1.5 kWp solar panel), which connect the dc source's positive and negative ends to the sink, respectively.

Fig. 16(a) presents the output voltage between the bridge legs of the SI-NPCTLI, referring to Fig. 1(b) and Table I. Fig. 16(b) gives the current waveforms of filter inductors L_1 and L_2, which indicates that they work half-cycle in a line period and have no bias current. Fig. 17 shows the gate drive voltage and the drain–source voltages of S_1 and S_2, respectively, in which voltage stress of S_1 is half of the PV input voltage, and the fact coincides with the principle; voltage stress of S_2 is the grid voltage and its maximum value is less than half of the PV input voltage.

Fig. 18(a) and (b) shows the common-mode current and its energy spectrum of the SI-NPCTLI and NPCTLI in the transformerless PV grid-connected applications, respectively. It is first pointed out that the common-mode path of the adjustable dc source is formed when the inverter connects to the grid, and the common-mode current $I_{18\,KHz}$ arises as the dc source works in the high-frequency switching (whose switching frequency is 18 kHz), while grid-connected inverter does not work yet. In the

two-stage grid-connected inverter, the high-frequency switching action of its front stage also generates a high-frequency common-mode current just like here (whether they contain a high-frequency transformer or not). So, the common-mode current $I_{18\,KHz}$ needs to be restrained, too. From the comparison of Fig. 18(a) and (b), both the SI-NPCTLI and the NPCTLI have suppress leakage current well.

VI. CONCLUSION

A split-inductor three-level grid-connected inverter with high reliability and low-leakage current characteristics is presented in this paper. The proposed inverter features low device voltage stress and constant common-mode voltage, which exists in the traditional neutral-point clamping three-level circuit structure. At the same time, it can avoid the shoot-through issue like a dual-buck half-bridge inverter. The proposed inverter can achieve high efficiency, low cost, low leakage current, and high reliability to satisfy the requirements of the transformerless PV

grid-connected inverter. The proposed structure can be also extended to three-phase four-line applications.

ACKNOWLEDGMENT

REFERENCES

[1] G. Petrone, G. Spagnuolo, R. Teodorescu, M. Veerachary, and M. Vitelli, "Reliability issues in photovoltaic power processing systems," *IEEE Trans. Ind. Electron.*, vol. 55, no. 7, pp. 2569–2580, Jul. 2008.

[2] H. Shinohara, K. Kimoto, T. Itami, T. Ambou, C. Okado, K. Nakajima, S. Hojo, K. Owada, M. Kuniyoshi, and Y. Sato, "Development of a residential use, utility interactive PV inverter with isolation transformer-less circuit—Development aspects," in *Proc. IEEE Photovolt. Spec. Conf.*, 1994, pp. 1216–1218.

[3] J. M. A. Myrzik and M. Calais, "String and module integrated inverters for single-phase grid connected photovoltaic systems—A review," in *Proc. IEEE Bologna Power Tech. Conf.*, 2003, pp. 1–8.

[4] M. Calais and V. G. Agelidis, "Multilevel converters for single-phase grid connected photovoltaic systems—An overview," in *Proc. IEEE Int. Symp. Ind. Electron.*, 1998, pp. 224–229.

[5] T. Kerekes, R. Teodorescu, and M. Liserre, "Evaluation of three-phase transformerless photovoltaic inverter topologies," *IEEE Trans. Power Electron.*, vol. 24, no. 9, pp. 2202–2211, Sep. 2009.

[6] A. Nabea, I. Takahashi, and H. Akagi, "A new neutral-point-clamped PWM inverter," *IEEE Trans. Ind. Appl.*, vol. 17, no. 5, pp. 518–523, Sep./Oct. 1981.

[7] E. Gubra, P. Sanchis, A. Ursua, J. Lopez, and L. Marroyo, "Ground currents in single-phase transformerless photovoltaic systems," *Prog. Photovolt.: Res. Appl.*, pp. 629–650, May 2007.

[8] R. Gonzalez, E. Gubia, J. Lopez, and L. Marroyo, "Transformerless single-phase multilevel-based photovoltaic inverter," *IEEE Trans. Ind. Electron.*, vol. 55, no. 7, pp. 2694–2702, Jul. 2008.

[9] H. F. Xiao and S. J. Xie, "Leakage current analytical model and application in single-phase transformerless photovoltaic grid-connected inverter," *IEEE Trans. Electromagn. Compat.*, vol. 52, no. 4, pp. 902–913, Nov. 2010.

[10] T. Kerekes, R. Teodorescu, and U. Borup, "Transformerless photovoltaic inverters connected to the grid," *Proc. IEEE Appl. Power Electron. Conf.*, pp. 1733–1737, 2007.

[11] N. R. Zargari, P. D. Zargari, and G. Joos, "A two switch high performance current regulated DC/AC converter module," *IEEE Trans. Ind. Appl.*, vol. 40, no. 1, pp. 162–169, Jan./Feb. 2004.

[12] R. S. Gerald and M. B. Kenneth, "Precision dc-to-ac power conversion by optimization of the output current waveform—The half-bridge revisited," *IEEE Trans. Power Electron.*, vol. 14, no. 2, pp. 372–380, Mar. 1999.

[13] J. Liu and Y. G. Yan, "Novel current mode controlled bi-buck half-bridge," *J. Nanjing Univ. Aeronaut. Astronaut.*, vol. 35, no. 2, pp. 122–126, Mar. 2003.

[14] C. H. Zhu and Y. G. Yan, "A novel series/parallel output dual buck inverter," in *Proc. Chin. Soc. Electr. Eng.*, Oct. 2005, vol. 25, no. 20, pp. 12–15.

[15] H. X. Ma, C. Y. Gong, and Y. G. Yan, "Output filter design of half-bridge dual-buck inverter using hysteresis current controller," in *Proc. Chin. Soc. Electr. Eng.*, Jul. 2007, vol. 27, no. 13, pp. 98–103.

[16] H. Z. Wang, Z. Q. Cai, J. Liu, and Y. G. Yan, "A novel three level dual buck half-bridge inverter," *Trans. China Electrotech. Soc.*, vol. 24, no. 2, pp. 73–77, Feb. 2009.

[17] Z. L. Yao, L. Xiao, and Y. G. Yan, "Dual-Buck full-bridge inverter with hysteresis current control," *IEEE Trans. Ind. Electron.*, vol. 56, no. 8, pp. 3153–3160, Aug. 2009.

[18] P. Bhagwat and V. Stefanovic, "Generalised structure of a multilevel PWM inverter," *IEEE Trans. Ind. Appl.*, vol. 19, no. 6, pp. 1057–1069, Nov./Dec. 1983.

[19] W. Jun and K. M. Smedley, "Synthesis of multilevel converters based on single- and/or three-phase converter building blocks," *IEEE Trans. Power Electron.*, vol. 23, no. 3, pp. 1247–1256, May 2008.

[20] M. Hagiware and H. Akagi, "Control and experiment of pulse-width-modulated modular multilevel converters," *IEEE Trans. Power Electron.*, vol. 24, no. 7, pp. 1737–1746, Jul. 2009.

[21] M. Shen, A. Joseph, J. Wang, F. Z. Peng, and D. J. Adams, "Comparison of traditional inverters and Z-source inverter for fuel cell vehicles," *IEEE Trans. Power Electron*, vol. 22, no. 4, pp. 1453–1463, Jul. 2007.

[22] A. Timbus, M. Liserre, R. Teodorescu, P. Rodriguez, and F. Blaabjerg, "Evaluation of current controllers for distributed power generation systems," *IEEE Trans. Power Electron.*, vol. 24, no. 3, pp. 654–664, Mar. 2009.

[23] M. A. S. Nejad, S. Pierfederici, and J. P. Martin, "Study of a hybrid current controller suitable for DC–DC or DC–AC applications," *IEEE Trans. Power Electron.*, vol. 22, no. 6, pp. 2176–2186, Nov. 2007.

[24] A. Shukla, A. Ghosh, and A. Joshi, "Improved multilevel hysteresis current regulation and capacitor voltage balancing schemes for flying capacitor multilevel inverter," *IEEE Trans. Power Electron.*, vol. 23, no. 2, pp. 518–529, Mar. 2008.

[25] L. Dalessandro, S. D. Round, and J. W. Kolar, "Center-point voltage balancing of hysteresis current controlled three-level PWM rectifiers," *IEEE Trans. Power Electron.*, vol. 23, no. 5, pp. 2477–2488, Sep. 2008.

[26] A. Schild, J. Lunze, J. Krupar, and W. Schwarz, "Design of generalized hysteresis controllers for dc–dc switching power converters," *IEEE Trans. Power Electron.*, vol. 24, no. 1, pp. 2484–2495, Jan. 2009.

[27] H. H. Huang, C. L. Chen, and K. H. Chen, "Adaptive window control (AWC) technique for hysteresis dc–dc buck converters with improved light and heavy load performance," *IEEE Trans. Power Electron.*, vol. 24, no. 6, pp. 1607–1617, Jun. 2009.

[28] C. N. M. Ho, V. S. P. Cheung, and H. S. H. Chung, "Constant-frequency hysteresis current control of grid-connected VSI without bandwidth control," *IEEE Trans. Power Electron.*, vol. 24, no. 11, pp. 2484–2495, Nov. 2009.
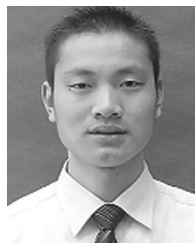
Huafeng Xiao (S'10) was born in Hubei, China, in 1982. He received the B.S., M.S. and Ph.D. degrees in electrical engineering from Nanjing University of Aeronautics and Astronautics, Nanjing, China, in 2004, 2007, and 2010, respectively.

In 2011, he joined the Faculty of Power Electronics, and is currently a Lecturer at the College of Electrical Engineering, Southeast University, Nanjing, China. His current research interests include high-frequency soft-switching conversion, photovoltaic applications, and application of power electronic technology in smart distribution grid. He is the author of more than 20 technical papers published in many international journals and conference proceedings.

Shaojun Xie (M'05) was born in Hubei, China, in 1968. He received the B.S., M.S. and Ph.D. degrees in electrical engineering from Nanjing University of Aeronautics and Astronautics (NUAA), Nanjing, China, in 1989, 1992 and 1995, respectively.

In 1992, he joined the Faculty of Electrical Engineering Teaching and Research Division, and is currently a Professor at the College of Automation Engineering, NUAA. He is the author of more than 50 technical papers published in many international journals and conference proceedings. His main research interests include aviation electrical power supply systems and power electronics conversion.